Research paper

Methane-dominated gaseous inclusions in the Sinian carbonate reservoirs in central Sichuan Basin and their implications for natural gas accumulation

Xing Wang [a,b], Hui Tian [a,*], Xianming Xiao [c], Dehan Liu [a], Yushun Min [a], Tengfei Li [a], Sui Ji [a], Ping'an Peng [a]

[a] State Key Laboratory of Organic Geochemistry, Guangzhou Institute of Geochemistry, Chinese Academy of Sciences, Guangzhou, 510640, China
[b] University of Chinese Academy of Sciences, Beijing, 100049, China
[c] China University of Geosciences, Beijing, 100083, China

ARTICLE INFO

ABSTRACT

The occurrence and genetic origins of gaseous inclusions in the Sinian carbonate reservoirs of Anyue gas field in central Sichuan Basin were investigated with techniques of micro-Raman spectroscopy and microthermometry to trace the oil and gas accumulation history. Three types of gaseous inclusions were identified in terms of their compositions and the homogenization temperatures (Ths) of their coeval aqueous inclusions. Both type I and type II gaseous inclusions are dominantly composed of methane with varying contents of pyrobitumen, indicating their origins of type I and II precursor oil inclusions that have been thermally converted to the present gaseous inclusions. The aqueous inclusions coeval with the present type I and type II gaseous inclusions have Th values in the range of 120.3–136.9 °C and 140.8–168.5 °C, respectively, further confirming that they are derived from precursor oil inclusions that were formed during 251–204 Ma and 202–169 Ma, respectively. For type III gaseous inclusions, their gaseous components are also dominated by methane with minor CO_2 and H_2S, but no detectable pyrobitumen is observed in them. This implies that they are not genetically related to any precursor oil inclusions but were formed by direct trapping of gases in reservoirs when the paleo-oil pools have been thermally converted to gas pools during the time of 153–103 Ma, which is consistent with the high Th values of 203.8–237.1 °C of their coeval aqueous inclusions.

The density of methane in gaseous inclusions was also estimated from methane Raman shifts. The respective values of methane density for types I, II and III gaseous inclusions vary from 0.262 to 0.293 g/cm^3 (avg. 0.272 g/cm^3), from 0.231 to 0.264 cm^3/g (avg. 0.247 g/cm^3), and from 0.231 to 0.293 cm^3/g (avg. 0.249 g/cm^3). Based on the density of methane in type III gaseous inclusions and the Th values of their coeval aqueous inclusions, their trapping pressures were calculated to be in the range of 93.3–134.1 MPa with formation pressure coefficients of 1.32–1.79. This indicates that there were overpressures in the reservoirs during the oil to gas cracking and that the almost hydrostatic system of the present Sinian gas pools is mostly related to the extensive tectonic uplift and subsequent loss of natural gas since late Cretaceous.

1. Introduction

The Anyue gas field is the largest gas field discovered in Sichuan Basin with proved reserves over 1.0×10^{12} m^3 (Zou et al., 2014a, 2020) and the reservoirs are mainly composed of dolomites of both the Sinian and Lower Cambrian successions (Zou et al., 2014b; Wei et al., 2015a, b; Wang et al., 2016; Zhao et al., 2018). The reservoirs were ever buried as deep as 8000 m during Cretaceous and experienced paleo-temperatures over 230 °C, and therefore the early accumulated oils in them have been thermally converted into natural gas and pyrobitumen (Zou et al., 2014a; Zhu et al., 2015; Chen et al., 2018; Gao et al., 2018; Liu et al., 2018). Although some authors suggested that gas generation from oil cracking in a relatively closed system may lead to considerable overpressure (Barker, 1990; Tian et al., 2008; Liu et al., 2010, 2016b), the present Sinian reservoirs are almost hydrostatically-pressured with formation pressure coefficients in the range of 1.06–1.14 (Liang et al.,

2016) while the overlying Lower Cambrian Longwangmiao reservoirs are now overpressured with a formation pressure coefficient of approximately 1.6 (Liu et al., 2016b, 2018). Early studies suggested that it was the more extensive loss of natural gas in the Sinian Dengying reservoirs than in the Lower Cambrian Longwangmiao reservoirs during the latest tectonic uplift that had led to their distinct pressure systems (Zou et al., 2014a; Liu et al., 2018). However, it is still not clear if there was ever overpressure in the Dengying reservoirs due to oil cracking before the extensive tectonic uplift during late Cretaceous to the present time.

In recent decades, gas-rich fluid inclusions have been paid much attention regarding their applications to understanding gas accumulation history (Burruss, 1998, 2003; Parris et al., 2003; Liu et al., 2010; Burruss et al., 2012; Fall et al., 2012; Lüders and Plessen, 2015; Huang et al., 2018; Bourdet et al., 2019; Volk and George, 2019). In particular, the methane density in CH_4-rich gaseous or aqueous inclusions can be estimated from microthermometric and/or Raman techniques (Thiéry et al., 2000; Goldstein, 2001; Chou et al., 2006; Lin et al., 2007; Lu et al., 2007; Becker et al., 2010; Zhang et al., 2016), which is then integrated with the homogenization temperatures (Ths) of their coeval aqueous inclusions to calculate the trapping pressure of such inclusions (Parris et al., 2003; Liu et al., 2010; Fall et al., 2012; Bourdet et al., 2019). For

instance, Parris et al. (2003) calculated the trapping pressure of CH_4-rich inclusions in Shublik Formation and Kingak Shale and investigated the relation of gas generation and accumulation history to the deformation in the Brooks Range foothills; Liu et al. (2010) observed a group of supercritical CH_4-dominated inclusions in the Triassic reservoirs in Puguang gas field, Sichuan Basin, and the maximum methane density of these inclusions was reported to be as high as up to 0.3477 g/cm^3, indicating a strong overpressure in the reservoirs during oil cracking; Fall et al. (2012) even illustrated that the CH_4-rich gaseous or aqueous inclusions can be applied to investigate the basin-centered, continuous gas accumulation history in southern Piceance Basin.

In this study, CH_4-dominated gaseous inclusions hosted in quartz grains in the carbonate reservoirs of Anyue gas field were analyzed with micro-Raman and microthermometric techniques. The main purpose of this study is to investigate their occurrence, origins, trapping temperatures and pressures, as well as their implications for the natural gas accumulation history in the Sinian carbonate reservoirs of the Anyue gas field.

2. Geological setting

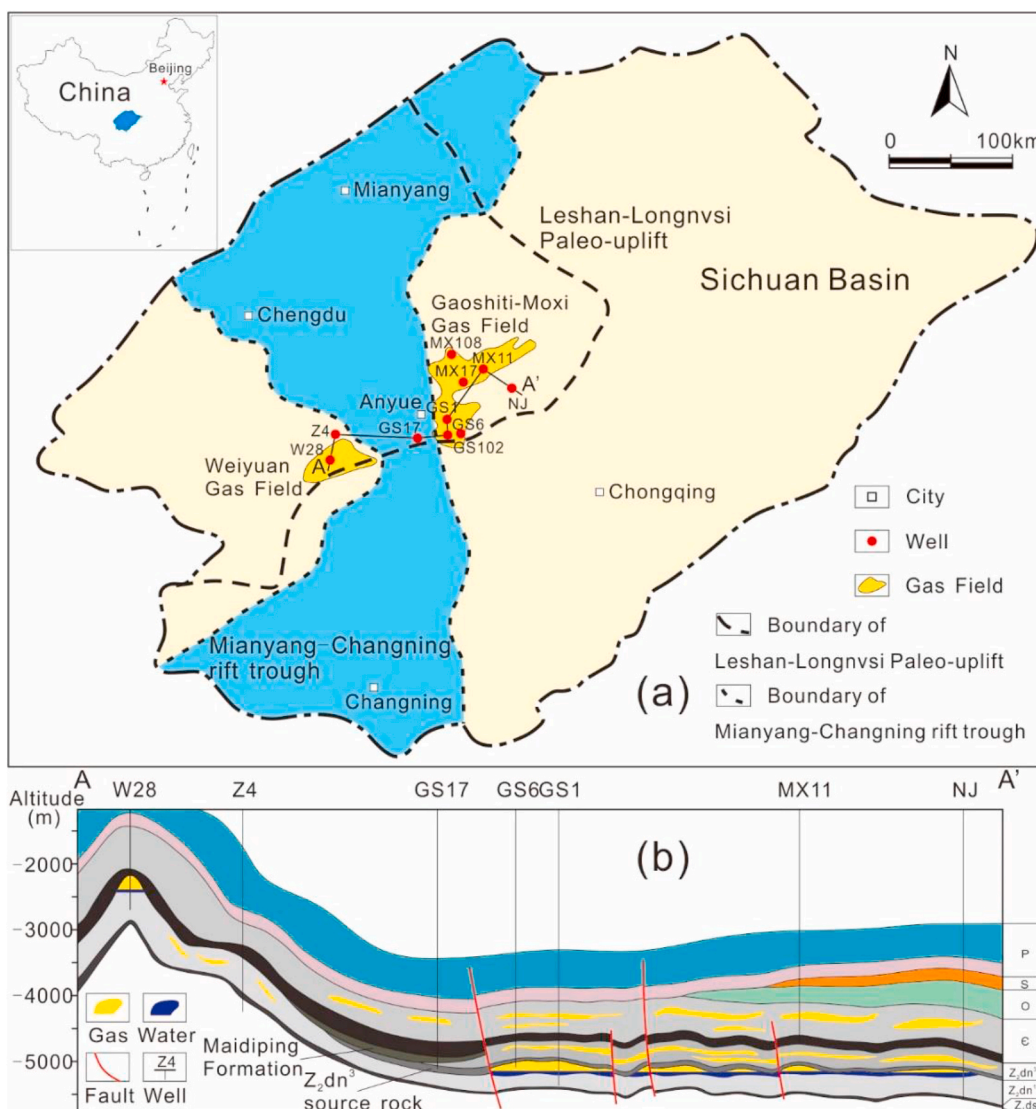As part of Upper Yangtze Block, Sichuan Basin is located in

Fig. 1. (a) Geological map of the main structure unit of Sichuan Basin (modified after Sun et al., 2017); (b) Cross-section of the study area (modified after Zou et al., 2014b; Zhu et al., 2015; Xu et al., 2018).

Southwest China (Fig. 1). The central part of Sichuan Basin, where the Weiyuan and Anyue gas fields are discovered, is bounded by the Longquan Mountain to the west and the Huaying Mountain to the east (Wei et al., 2013; Liu et al., 2016b). In this area, an inherited paleo-uplift named Leshan-Longnvsi paleo-uplift was initially shaped during late Ediacaran and finally formed at late Silurian (Wei et al., 2013; Mei et al., 2014). To the west of Leshan-Longnvsi paleo-uplift, a north-south-trend rift trough, i.e., the Mianyang-Changning (MC) rift trough (Fig. 1), has been discovered and is believed to have been formed during the early

Cambrian (Song et al., 2013; Zou et al., 2014a; Sun et al., 2017). To the east of the MC rift trough is the Weiyuan-Ziyang (WZ) Bulge, while the Moxi-Gaoshiti (MG) Bulge is on the west (Fig. 1).

Sichuan Basin has experienced multiple tectonic movements. The Tongwan movement resulted in two unconformities within the Dengying Formation, and one is between the second and third members and the other is between the fourth member of Dengying Formation and the Lower Cambrian strata (Fig. 2; Mei et al., 2014; Wang et al., 2014b; Duan et al., 2019). The Caledonian movement extensively shaped the
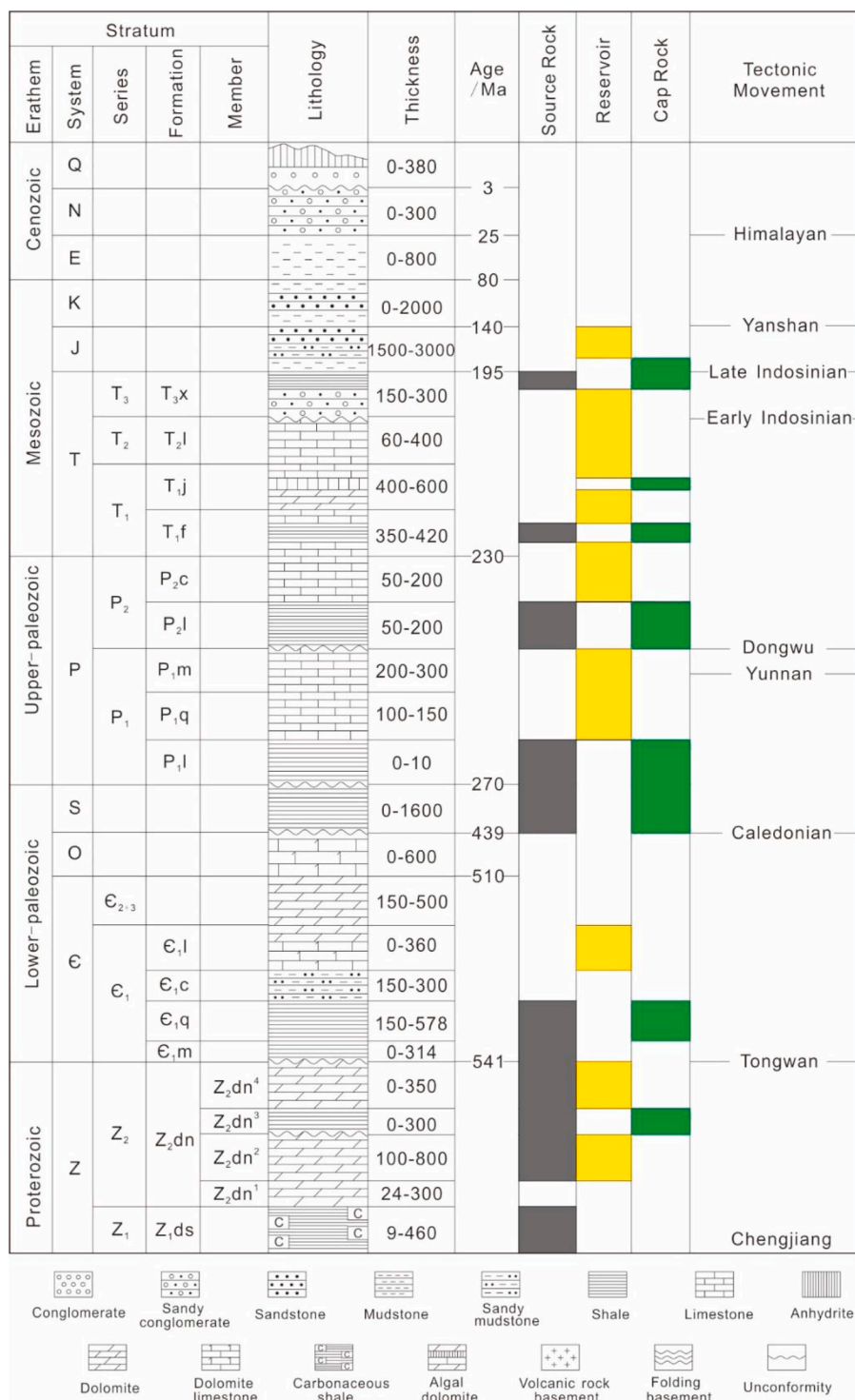

Fig. 2. Generalized stratigraphy and assemblage of source rocks, reservoirs and seals in the Moxi-Gaoshiti Bulge (modified after Xu et al., 2012; Zhu et al., 2015; Liu et al., 2016b).

Sichuan Basin, leading to the total erosion of the Devonian and Carboniferous sequences in the study area. Entering the Permian, the basin subsided again and received sequences of both clastic and carbonate rocks during the Hercynian to early Yanshanian until it was uplifted during the late Yanshanian to Himalayan period (Fig. 2; Yuan et al., 2013; Sun et al., 2017). During this period, the WZ Bulge was uplifted more intensely than the MG Bulge, finally forming the present tectonic pattern (Fig. 1b; Zhu et al., 2009; Mei et al., 2014).

The petroleum system of the Anyue gas field involves both the Sinian and Cambrian successions (Fig. 2). The Lower Cambrian Qiongzhusi black shale is the main source rocks with an average TOC value of 1.93% and thickness of 140 m (Zou et al., 2014b). The second and fourth members of the Dengying Formation are the main gas reservoirs, which are dominated by algal dolomite with a total thickness of around 240 m (Fig. 2; Zou et al., 2014b; Shi et al., 2018). Both the Qiongzhusi Formation and the second and fourth members of the Dengying Formation have equivalent vitrinite reflectance (EqVRo) values greater than 2.0%, indicating a dry gas stage (Zou et al., 2014a, b; Wei et al., 2015b; Zhu et al., 2015; Liu et al., 2018; Xu et al., 2018). The Longwangmiao Formation, another major reservoirs of the Anyue gas field, is also dominated by dolomite (Fig. 2; Zou et al., 2014; Zhang et al., 2018). The schematic assemblages of source rocks, reservoirs and sealing rocks are presented in Fig. 2.

3. Samples and methods

3.1. Samples

Core samples used in this study were collected from the fourth member of Dengying Formation (Fig. 2) of wells Gaoshi 6, Gaoshi 102, Moxi 17, Moxi 102 and Moxi 110. All these wells are located in the MG Bulge (Fig. 1), and the depths of collected samples are in the range of 5039.3–5375.9 m (Table 1).

3.2. Pyrobitumen reflectance

The pyrobitumen reflectance was measured on a 3Y Leica DMR XP microphotometer. Given that the studied samples are of high-to overmaturity, a Cubic Zirconia standard with a reflectance value of 3.11% was used to calibrate the instrument. A 50 × oil-immersion objective

Table 1
Geological and geochemical information of samples.

Well name	Depth (m)	Sample	[a]BR$_o$ (%)	[b]BR$_o$ (%)	[c]BR$_o$ (%)
Gaoshi6	5366.3	GS6-1	2.51–4.68/ 3.85(23)	–	3.74–3.78/ 3.76(5)
Gaoshi102	5039.3	GS102-1	2.89–5.22/ 3.66(34)	–	3.71–3.73/ 3.72(5)
	5069.6	GS102-2	2.17–5.11/ 3.66(40)	3.56–3.77/ 3.63(14)	3.72–3.79/ 3.75(5)
	5126.9	GS102-3	2.27–5.08/ 3.57(40)	–	3.74–3.78/ 3.76(5)
Moxi17	5076.5	MX17-1	2.22–5.19/ 3.62(40)	–	3.74–3.78/ 3.76(5)
Moxi102	5190.6	MX102-1	2.09–5.29/ 3.59(40)	–	3.70–3.75/ 3.73(5)
Moxi110	5375.9	MX110-1	2.56–4.46/ 3.52(40)	–	3.71–3.73/ 3.72(5)

[a] Measured reflectance of pyrobitumen in reservoirs.
[b] Bitumen reflectance (BRo) calculated from the *Graphite* and *Disorder* Raman peaks of pyrobitumen in Type I gaseous inclusions using the equation BRo% = 1.67 × (I_D/I_G)+2.58 (Wang et al., 2015), I_D and I_G are the Raman intensity of *Disorder* and *Graphite* peaks, respectively.
[c] Bitumen reflectance (BRo) calculated from the *Graphite* and *Disorder* Raman peaks of pyrobitumen in reservoirs using the equation BRo% = 1.67 × (I_D/I_G)+ 2.58 (Wang et al., 2015), I_D and I_G are the Raman intensity of *Disorder* and *Graphite* peaks, respectively.

was used to measure the pyrobitumen reflectance.

3.3. Microthermometry and Raman of fluid inclusions

Double-polished thin sections were prepared for fluid inclusion examination. Petrological observation of fluid inclusions were performed on a Leica DMR XP microscope with objective lens of 2.5–100 × . The homogenization temperature of fluid inclusions was determined on a THMS-Q600 instrument. The rate of heating or cooling was set as 0.5–20 °C/min and controlled by the Linkham Scientific LINKSYS 32 software.

The Raman spectrum analysis of pyrobitumen and gaseous fluid inclusions was conducted on a HORIBA-JY LabRAM Aramis Raman system equipped with a Nd: YAG laser. The laser has an excitation wavelength of 532.06 nm, and a grating of 1800 grooves/mm with a slit width of 100 μm was used. During experiments, the Raman shifts in the range of 100–4300 cm^{-1} were collected with exposure time 10–20 s.

The measured Raman shift of methane was calibrated by a Neon lamp, using the method suggested by Zhang et al. (2016):

$$\frac{\nu_{\text{ture}} - 2836.99}{\nu_{\text{mea}} - Ne_1} = \frac{3008.13 - 2836.99}{Ne_2 - Ne_1} \tag{1}$$

Where, the ν_{true} and ν_{meas} represent the true and measured value of methane Raman shift, respectively; Ne_1 and 2836.99 respectively represent the measured and theoretical Raman shift of Neon lamp at 626.65 nm, and Ne_2 and 3008.13 are the measured and theoretical Raman shift at 633.44 nm, respectively.

Methane density in methane-dominated inclusions was calculated by its Raman shift following the equation proposed by Lu et al. (2007):

$$\rho\left(g / cm^3\right) = -5.17331 \times 10^{-5}D^3 + 5.53081 \times 10^{-4}D^2 - 3.51387 \times 10^{-2}D \tag{2}$$

Here, $D = \nu_{\text{true}} - \nu_0$, and ν_0 is the Raman shift of methane at near zero pressure. In this study, the ν_0 value was determined by directly measuring the methane Raman shift in a doubly sealed capillary where the pressure of sealed methane is approximately 0.1 MPa (Chou et al., 2006), and the value is 2918.21 cm^{-1} after neon-lamp correction.

When the methane-dominated inclusions are large enough and clear to observe, the methane density (ρ) in them was also estimated from their homogenization temperatures (T_h) using the method proposed by Rackett (1970) and Liu (2005):

$$V_h = V_c Z_c^{(1-T_r)^{2/7}} \tag{3}$$

Here, V_h is the homogenization volume of methane-dominated fluid inclusion (cm^3/mol); V_c is the critical molar volume of methane (98.63 cm^3/mol); Z_c is the critical compressibility factor (0.2864 for methane); T_r is the ratio of measured homogenization temperature (T_h) to the critical temperature (T_c) of methane (190.55 K),

$$T_r = T_h/T_c \tag{4}$$

The methane density was calculated by the molar mass of methane ($M = 16.0426$ g/mol) and the homogenization volume V_h:

$$\rho = M/V_h \tag{5}$$

4. Results and discussion

4.1. Petrology of carbonate reservoirs

The Sinian carbonate reservoir is mainly composed of dolomites where micro-fractures and dissolution pores are widely developed with filling minerals of dominantly quartz and calcite (Fig. 3). The quartz in reservoirs can be visually divided into two types. The first type is characterized by quartz aggregates with different regions and has diameters from hundreds of micrometers to several millimeters (Fig. 3a);
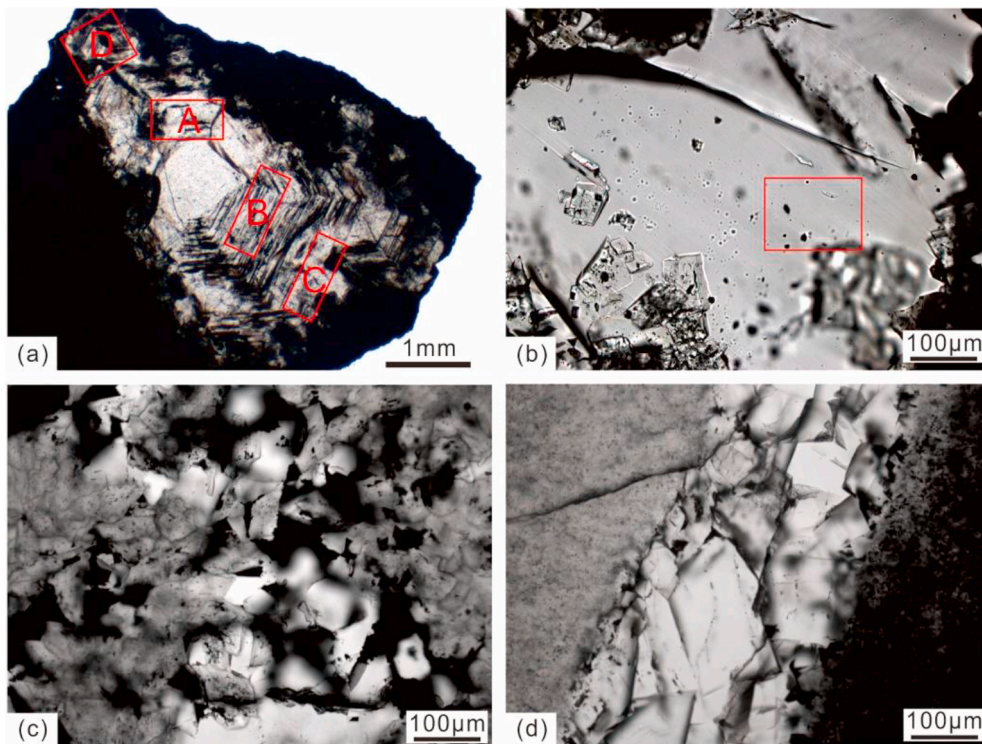
Fig. 3. Petrologic features of Sinian carbonate reservoirs. (a): quartz grainassemblage hosting fluid inclusions in different regions in dolomite matrix, sample GS102-2; (b): xenomorphic quartz cement in dolomite matrix, sample GS102-3. The red panel indicates the scope of Fig. 5c; (c): xenomorphic quartz cement and pyrobitumen in dolomite matrix, sample MX17-1; (d): calcite veins filling early formed fractures in dolomite matrix, sample GS6-1.
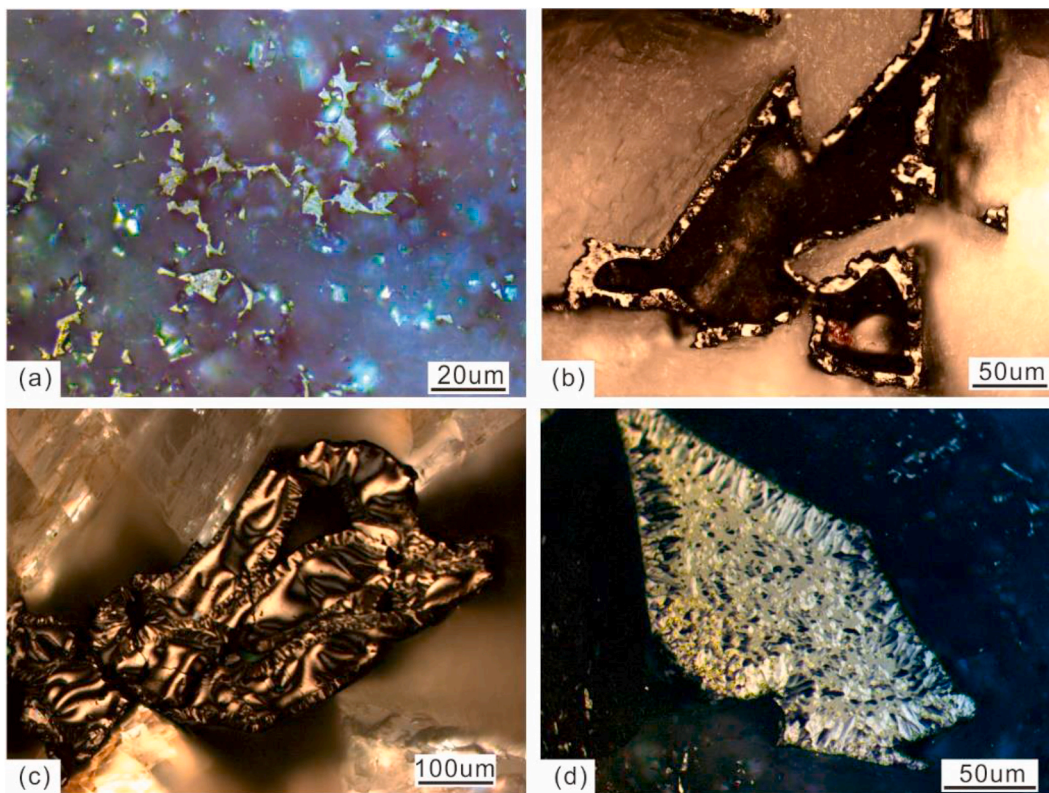

Fig. 4. Pyrobitumen characteristics in Sinian carbonate reservoirs. (a) intergranular pyrobitumen, sample MX110-1; (b) pyrobitumen lining the edge of dissolution pores, sample GS102-1; (c) fibrous pyrobitumen, sample GS102-2; (d) fine to medium mosaic pyrobitumen, sample MX110-1.

the other type of quartz grains usually have xenomorphic shapes with diameters of several to tens of micrometers (Fig. 3b and c). The calcite grains in fractures may show banded structures along the fracture but usually have irregular shapes (Fig. 3d).

Microscopic examination of thin sections reveals that pyrobitumen is widely distributed either between mineral grains or within dissolution pores. The intergranular pyrobitumen usually has irregular shapes with diameters of several to tens of micrometers (Fig. 4a), whereas the pyrobitumen in dissolution pores is larger with diameters from tens of micrometers to several millimeters (Fig. 4b–d). The pyrobitumen lining dissolution pores (Fig. 4b) is an indicator of thermal cracking of early accumulated oils in the pores, and the presence of fibrous texture (Fig. 4c) as well as the fine to medium mosaic texture (Fig. 4d) in pyrobitumen indicate extremely high thermal maturity due to the very high temperatures suffered by the Sinian reservoirs (Gao et al., 2018; Yang et al., 2018). The measured random pyrobitumen reflectance (BRo) values for each sample have a wide range due to the strong anisotropy of highly matured pyrobitumen and for examples, the BRo values vary from 2.09 to 5.29% for sample MX102-1 (Table 1). However, the mean BRo values for different samples are quite identical and range from 3.52 to 3.85% (Table 1), indicating that all samples have experienced similar thermal maturation. Based on the equation suggested by Schoenherr et al. (2007), the BRo values correspond to EqVRo values of 3.59–3.90%. In addition, the thermal maturity of pyrobitumen was further examined in terms of their separation of *Graphite* and *Disorder* Raman shifts. Following the equation suggested by Wang et al. (2015), the Raman-based BRo values of pyrobitumen vary from 3.72 to 3.76%, close to the measured BRo values (Table 1).

4.2. Occurrence and genetic types of fluid inclusions

In general, fluid inclusions in our samples were observed in varying minerals such as dolomite, quartz and calcite (Table 2). In terms of their components, most fluid inclusions fall into gaseous (Fig. 5a–d), pyrobitumen (Fig. 5e) and two-phase aqueous inclusions (Fig. 5a–d); occasionally three-phase inclusions with daughter pyrobitumen were observed (Fig. 5f). Gaseous inclusions were mostly identified in quartz grains, and can be divided into three types according to their components and Raman shift of methane (Figs. 6 and 7).

4.2.1. Type I gaseous inclusions

Type I gaseous inclusions are mainly composed of methane with high abundance of pyrobitumen (Figs. 5a, 6a and 6b) and mostly developed in the Region B of the quartz aggregates of sample GS102-2 (Fig. 3a).

Table 2
Occurrence of different types of gaseous inclusions and the homogenization temperatures of their coeval aqueous inclusions.

Sample	Hosted mineral	Types of gaseous inclusion	Homogenization temperature of (coeval) aqueous inclusion
GS6-1	Dolomite	–	123.0–131.4/128.8(4)
GS102-2	Region A of quartz aggregates	–	118.5–133.2/127.7(5)
GS102-2	Region B of quartz aggregates	Type I	120.3–136.9/125.6(8)
GS102-2	Region C of quartz aggregates	Type II	140.8–168.5/154.3(15)
GS102-2	Region D of quartz aggregates	–	197.1–223.2/208.3(9)
GS102-3	Xenomorphic quartz	Type III	210.8–237.1/222.4(4)
MX17-1	Xenomorphic quartz	Type III	203.8–225.7/214.1(3)
MX102-1	Calcite	–	168.5–181.6/174.7(4)
MX110-1	Calcite	–	159.7–176.8/170.7(5)

These inclusions have sizes of 2–8 μm, usually display negative crystal structure and are opaque to semitransparent in transmitted light (Fig. 5a). The highly abundant pyrobitumen in them is evidenced by the strong *Disorder* (1320–1330 cm^{-1}) and *Graphite* (1600–1610 cm^{-1}) Raman peaks (Fig. 6a); meanwhile the gaseous components in them are dominated by methane with minor CO_2 (Fig. 6a). The measured Raman shifts of methane in type I gaseous inclusions are in the range 2911.16–2911.79 cm^{-1}, with an average of 2911.58 cm^{-1} (Fig. 7a; Table 3). Two-phase aqueous inclusions coeval with types I gaseous inclusions were also observed and usually have negative crystal structures with diameters of 2–8 μm (Fig. 5a).

The coexistence of pyrobitumen and methane type I gaseous inclusions indicates that they are derived from precursor oil inclusions (denoted as type I) that were formed during oil charge events and then thermally converted to the present gaseous inclusions, a process that resembles the oil to gas cracking in reservoirs. This interpretation is supported by two lines of evidence. Firstly, the Th values of their coeval aqueous inclusions range from 120.3 to 136.9 °C (Table 3), under which temperatures the oils in reservoirs are thermally stable (Waples, 2000); secondly, the BRo values of pyrobitumen in type I gaseous inclusions were calculated to be approximately 3.63% in terms of the separation of *Graphite* and *Disorder* peaks using the equation of Wang et al. (2015), which is quite similar to those for the pyrobitumen in reservoirs (Table 1). This indicates that the pyrobitumen both in reservoirs and in type I gaseous inclusions have experienced the same thermal history.

4.2.2. Type II gaseous inclusions

Type II gaseous inclusions, mainly identified in the Region C of the quartz aggregates of sample GS102-2 (Fig. 3a), are also dominated by methane but contain less abundant pyrobitumen (Fig. 5b) than type I gaseous inclusions as illustrated by their Raman spectra (Fig. 6c and d); they have sizes ranging from 5 to 15 μm (Fig. 5b), and commonly with round or subround shapes and occasionally displaying negative crystal structure or irregular shapes. Some coeval two-phase aqueous fluid inclusions are also developed, usually round or subround with diameters of 2–10 μm (Fig. 5b).

The gaseous components in type II gaseous inclusions, as indicated by their Raman spectra, are also dominated by methane with minor CO_2, which are similar to those of type I gaseous inclusions. The measured Raman shifts of methane in them range from 2911.76 to 2912.43 cm^{-1}, averaging at 2912.10 cm^{-1} (Figs. 6c and 7b and Table 3). The Raman spectra of pyrobitumen in type II gaseous inclusions also show *Graphite* and *Disorder* peaks, but they are much weaker than those for type I gaseous inclusions (Fig. 6c). This indicates that type II gaseous inclusions contain less abundant pyrobitumen than type I gaseous inclusions, and therefore are more transparent (Fig. 5a and b).

Like type I gaseous inclusions, type II gaseous inclusions are also interpreted to be related to the thermal conversion of precursor oil inclusions (denoted as type II). However, the type II precursor oil inclusions likely have lower bulk oil densities than type I precursor oil inclusions due to their reduced pyrobitumen content. This is because that the thermal cracking of low-density oils usually yields less pyrobitumen than high-density oils (Huc et al., 2000). Moreover, the aqueous inclusions coeval with type II gaseous inclusions have Th values in the range of 140.8–168.5 °C, also indicating that type II precursor oil inclusions were formed later than type I precursor oil inclusions. The oils in such reservoir temperatures can still be preserved as an independent phase but will have a high gas to oil ratio (Waples, 2000), which subsequently reduces the bulk density of reservoired oils.

4.2.3. Type III gaseous inclusions

Unlike types I and II gaseous inclusions, type III gaseous inclusions are single-phase and show no pyrobitumen signals in their Raman spectra (Fig. 6e and f). They usually have subround to irregular shapes with 2–12 μm length, and are mostly formed in xenomorphic quartz grains with semitransparent to transparent color in transmitted light
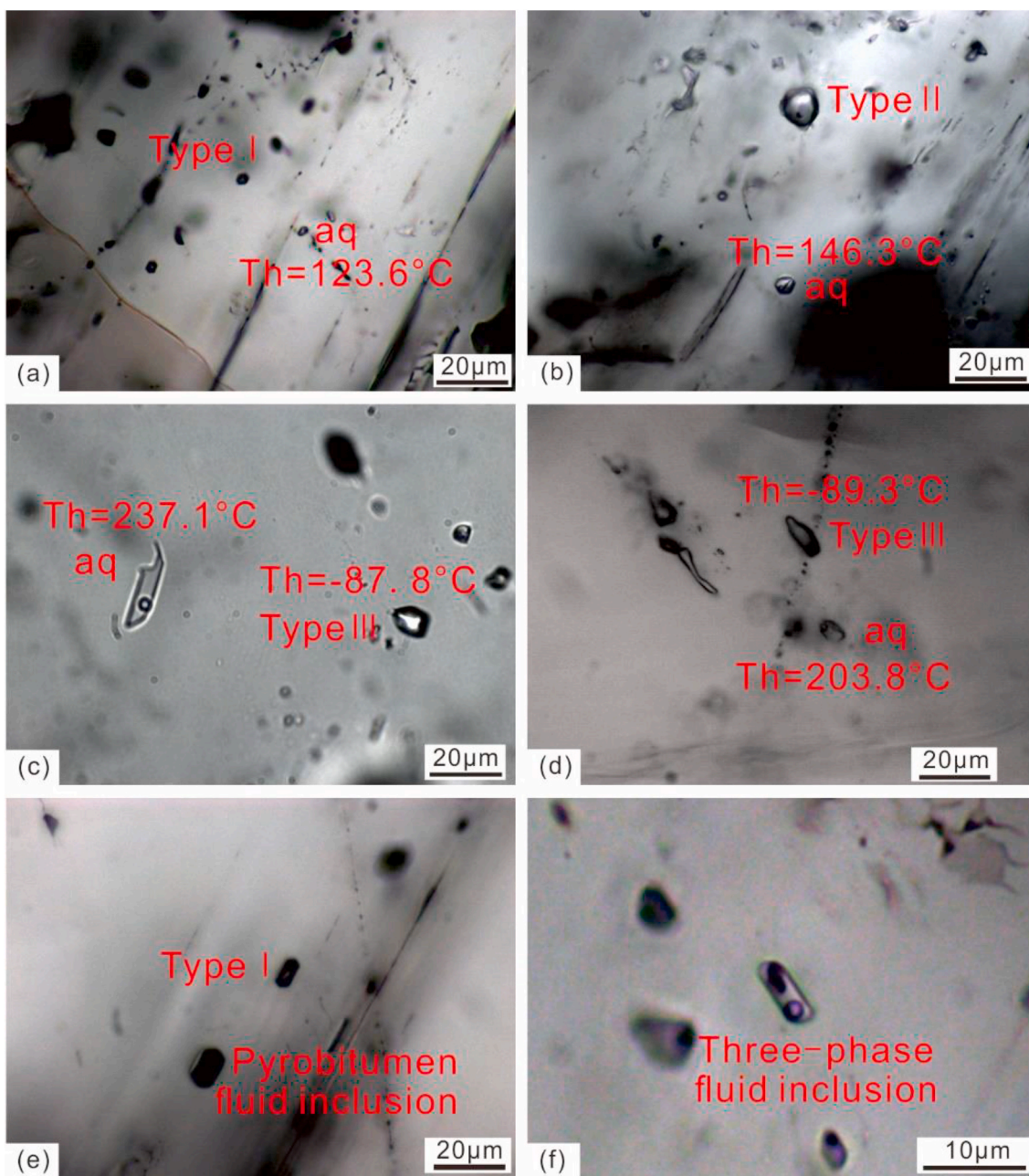
Fig. 5. Microphotographs showing different types of fluid inclusions hosted in quartz in Sinian reservoirs of MG Bulge. (a) Type I gaseous inclusions with negative crystal shape and their coeval aqueous fluid inclusions in Region B of quartz aggregates shown in Fig. 3a, sample GS102-2; (b) Type II gaseous inclusion and coeval aqueous fluid inclusion in Region C of quartz aggregates shown in Fig. 3a, sample GS102-2; (c) Type III gaseous inclusion and its coeval aqueous fluid inclusion in xenomorphic quartz, sample GS102-3; (d) Type III gaseous inclusion and its coeval aqueous fluid inclusion in xenomorphic quartz, sample MX17-1; (e) Coeval type I gaseous inclusions and pyrobitumen inclusion in Region B of quartz aggregates shown in Fig. 3a, sample GS102-2; (f) Three-phase fluid inclusion in Region C of quartz aggregates shown in Fig. 3a, sample GS102-2.

(Fig. 5c and d). The components of type III gaseous inclusions are dominated by methane with minute CO_2 and H_2S (Fig. 6e and f). The measured Raman shifts of methane in them vary between 2911.16 and 2912.38 cm^{-1} for sample GS102-3, and from 2911.79 to 2912.43 cm^{-1} for sample MX17-1 (Fig. 7c and d and Table 3). The absence of pyrobitumen in type III gaseous inclusions implies that they are not genetically related to any precursor oil inclusions but most likely formed by a direct trapping of the gases in reservoirs when the paleo-oils were thermally cracked to gas and pyrobitumen. This interpretation is supported by the high Th values of 203.8–237.1 °C (avg. 218.8 °C) for their coeval aqueous inclusions, which are high enough for thermal conversion of reservoired oil to gas (Schenk et al., 1997; Waples, 2000; Tian

et al., 2008). In addition, these high Th values are also consistent with the thermal maturity level reflected by pyrobitumen reflectance (Zou et al., 2014a; Gao et al., 2018; Liu et al., 2018; Yang et al., 2018).

It is worthy to note that many experimental results suggested that at the temperature of 203.8 °C, the natural gas generated from oil cracking contains high content of wet gas (Behar et al., 1992; Horsfield et al., 1992; Schenk et al., 1997; Tian et al., 2012). In Sichuan Basin, however, the oil cracking gas is usually methane-dominated at this temperature. For example, the Lower Triassic natural gas in the eastern Sichuan Basin is believed to be derived from oil cracking and usually has very high dryness indices of greater than 0.99 (Ma et al., 2007; Liu et al., 2010). The Th values of aqueous inclusions that are coeval with the
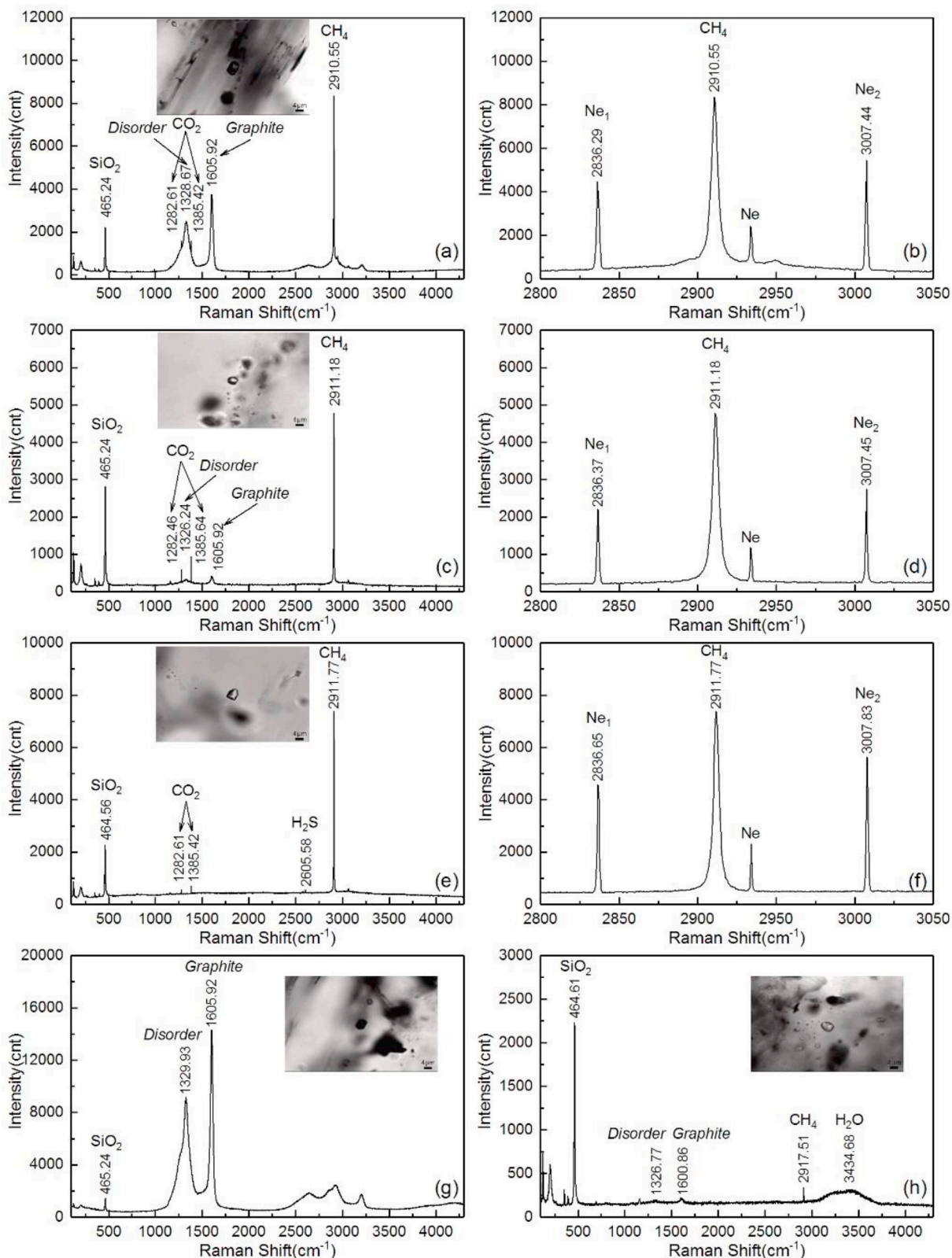
Fig. 6. Raman spectra of typical gaseous inclusions. (a): Raman spectrum of type I gaseous inclusions, sample GS102-2; (b): partial Raman spectrum of (a) with Neon lamp; (c): Raman spectrum of type II gaseous inclusions, sample GS102-2; (d): partial Raman spectrum of (c) with Neon lamp; (e): Raman spectrum of type III gaseous inclusion in xenomorphic quartz, sample GS102-3; (f): partial Raman spectrum of (e) with Neon lamp; (g): Raman spectrum of pyrobitumen inclusion, sample GS102-2; (h): Raman spectrum of three-phase inclusion, sample GS102-2.
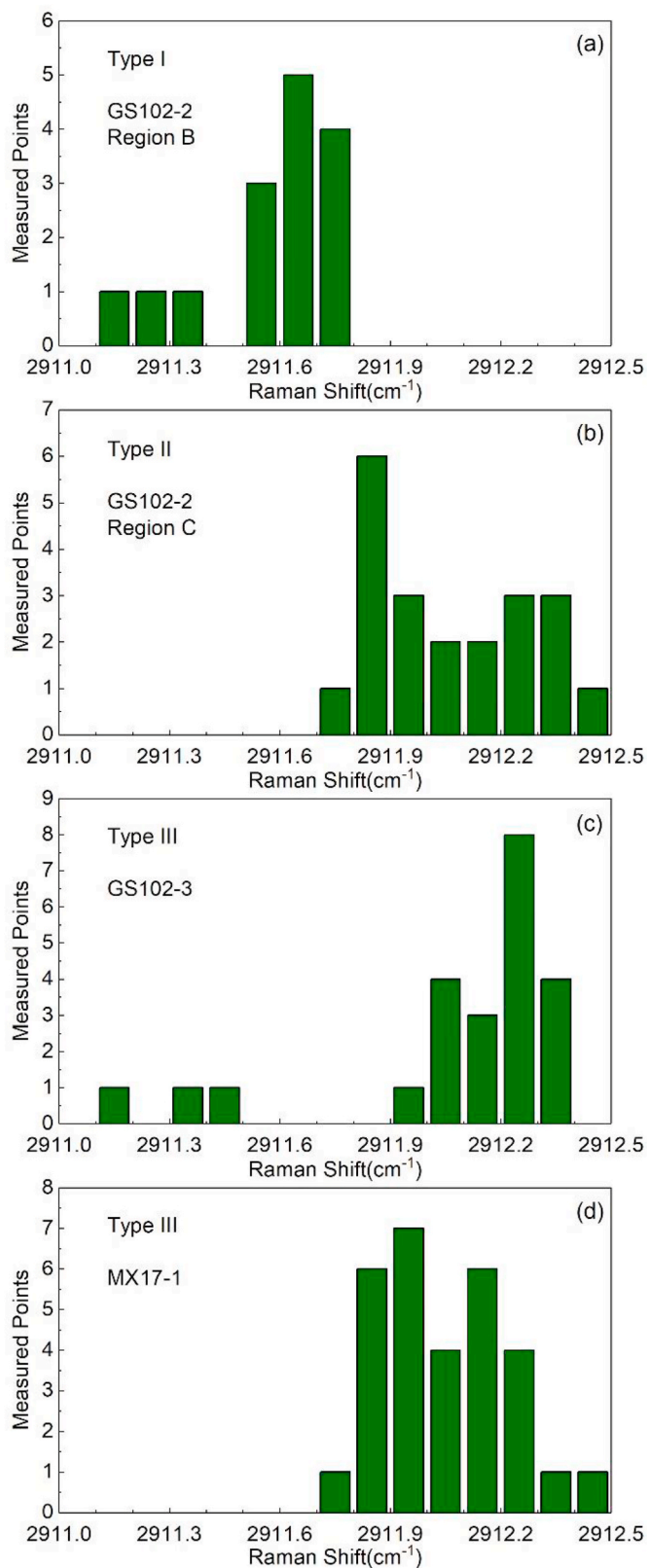
Fig. 7. Histograms showing the distribution of measured methane Raman shifts for different types of gaseous inclusions. (a): type I gaseous inclusions hosted in Region B shown in Fig. 3a, sample GS102-2; (b): type II gaseous inclusions in Region C shown in Fig. 3a, sample GS102-2; (c) and (d): type III gaseous inclusions in samples GS102-3 and MX17-1, respectively.
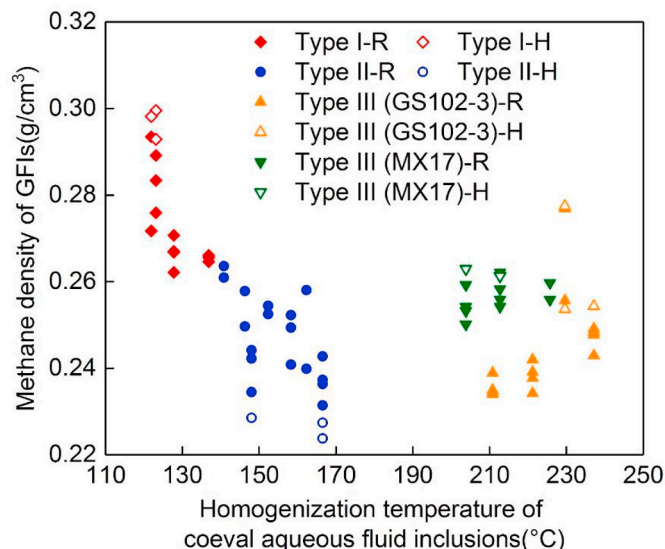

Fig. 8. Density values of methane in different types of gaseous inclusions developed in aggregated quartz and fractures (-R and H means the calculation according to Raman shifts of methane and the homogenization temperature of gaseous inclusions, respectively).

single-phase methane inclusions in Puguang gas field are only 185–200 °C (Liu et al., 2010). This is likely attributed to the thermal sulfate reaction (TSR) that accelerates the reactions of oil to gas cracking, which is evidenced by the varying amounts of H_2S in the Lower Triassic reservoirs and the Sinian Dengying reservoirs (Liu et al., 2010, 2016a).

4.2.4. Pyrobitumen inclusions and three-phase inclusions

In regions B and C of the quartz aggregates of sample GS102-2 (Fig. 3a), pyrobitumen inclusions and three-phase inclusions were also identified. The pyrobitumen inclusions can be round or subround and sometimes have negative crystal structure with sizes of 2–10 μm (Fig. 5e); they are usually coeval with types I and type II gaseous inclusions but contain no gaseous components (Fig. 6g). The pyrobitumen inclusions are most likely derived from the decrepitation of type I or type II gaseous inclusions in light of their coeval occurrence, and this phenomenon is quite common when the internal pressure in fluid inclusion is too high (Vityk and Bodnar, 1995; Goldstein, 2001). Alternatively some of the pyrobitumen inclusions in Region B of quartz aggregates may be related to precursor oil inclusions that were formed earlier than either type I or type II precursor oils inclusions. In such a case, the earliest precursor oil inclusions are expected to contain oils having much lower gas to oil ratios and thus a high oil density, and their thermal cracking may have generated very high internal pressures that are large enough to decrepitate the inclusions.

The three-phase inclusions are often round or subround, occasionally displaying negative crystal structure, and vary between 3 and 12 μm in size (Fig. 5f). The presence of pyrobitumen, gas bubbles as well as water in them is readily revealed by their Raman spectra, and the gas bubble is dominated by methane (Figs. 5f and 6h). They can be interpreted to be derived from the early trapped immiscible oil and aqueous inclusions, and hence the oils in them were cracked into pyrobitumen and methane under severe thermal stress, finally forming the present three-phase inclusions.

4.3. Density of methane in gaseous inclusions

The density of methane in gaseous inclusions was determined in terms of the methane Raman shift corrected with neon lamp, and the results are summarized in Table 3. In general, the methane in type I

Table 3
Raman shift and density of methane in typical gaseous inclusions.

Type of gaseous inclusion	Sample	Host mineral	Homogenization temperature of coeval aqueous inclusion	Measured Raman shift of methane (/cm^{-1})	Raman shift of methane corrected by Neon lamp (cm^{-1})	[a] Methane density (g/cm^3)	Homogenization temperature (°C)	[b] Methane density (g/cm^3)
Type I	GS102-2	Region B of quartz aggregates	122.7; 123.6	2910.55–2910.87/2910.70(3)	2911.24–2911.51/2911.37(3)	0.276–0.289/0.283(3)	−96.2; −98.1	0.293; 0.300
			120.3–123.3/121.9 (3)	2910.59–2911.06/2910.86(3)	2911.16–2911.59/2911.45(3)	0.272–0.293/0.279(3)	−97.7	0.298
			126.1; 129.5	2911.06–2911.17/2911.10(5)	2911.61–2911.79/2911.70(5)	0.262–0.271/0.267(5)	–	–
			136.9	2911.07–2911.18/2911.14(3)	2911.71–2911.74/2911.72(3)	0.265–0.266/0.265(3)	–	–
			—[c]	2910.99	2911.61	0.271	–	–
Type II	GS102-2	Region C of quartz aggregates	152.8–168.5/158.3 (3)	2911.32–2911.52/2911.43(3)	2911.99–2912.23/2912.09(3)	0.241–0.252/0.247(3)	–	–
			146.3–150.1/148.0 (3)	2911.52–2911.82/2911.66(3)	2912.16–2912.37/2912.24(3)	0.234–0.244/0.240(3)	−84.6	0.229
			164.6; 168.5	2911.45–2911.72/2911.62(4)	2912.31–2912.43/2912.32(4)	0.231–0.243/0.237(4)	−84.2; −84.5	0.224; 0.227
			142.0; 150.6	2911.34; 2911.36	2911.88; 2912.05	0.250; 0.258	–	–
			157.9; 166.7	2911.22; 2911.74	2911.87; 2912.25	0.240; 0.258	–	–
			140.8	2911.22; 2911.22	2911.76; 2911.81	0.261; 0.264	–	–
			145.6; 159.2	2911.36; 2911.38	2911.95; 2911.99	0.252; 0.254	–	–
			—[c]	2911.43–2911.64/2911.55(3)	2911.85–2912.23/2912.06(3)	0.241–0.259/0.249(3)	–	–
Type III	GS102-3	Xenomorphic quartz	229.6	2910.86; 2913.57	2911.49; 2911.92	0.256; 0.277	−92.3; −87.7	0.254; 0.277
			212.2	2911.56–2911.69/2911.64(4)	2912.21–2912.37/2912.29(4)	0.234–0.242/0.238(4)	–	–
			237.1	2911.43–2913.98/2912.22(4)	2912.06–2912.19/2912.10(4)	0.243–0.249/0.247(4)	−87.8	0.254
			210.8	2911.59–2911.77/2911.68(4)	2912.27–2912.38/2912.34(4)	0.234–0.239/0.236(4)	–	–
			—[c]	2911.55–2913.66/2911.88(9)	2911.16–2912.29/2912.34(9)	0.238–0.293/0.254(9)	−92.3 to −90.2/−90.2(3)	0.268–0.277/0.274(3)
	MX17-1	Xenomorphic quartz	203.8	2911.18–2913.64/2911.95(4)	2911.85–2912.04/2911.95(4)	0.250–0.259/0.254(4)	−89.3	0.263
			225.7	2911.21; 2911.33	2911.84; 2911.92	0.256; 0.260	–	–
			212.7	2911.18–2913.67/2911.85(4)	2911.79–2911.95/2911.88(4)	0.254–0.262/0.258(4)	−89.0	0.261
			—[c]	2911.33–2913.64/2911.73(20)	2911.89–2912.43/2912.13(20)	0.231–0.257/0.246(20)	−86.9	0.248

[a] Calculated by the Raman shifts of methane.
[b] Calculated by the homogenization temperatures of gaseous inclusions.
[c] Gaseous inclusions that have no coeval aqueous fluid inclusions.

gaseous inclusions has the highest density, ranging from 0.262 to 0.293 g/cm^3 with an average of 0.272 g/cm^3; the methane density values for type II gaseous inclusions vary between 0.231 and 0.264 g/cm^3 with an average of 0.247 g/cm^3; for type III gaseous inclusions, their methane density values are in the range of 0.231–0.293 g/cm^3 (avg. 0.249 g/cm^3), slightly higher than those of type II gaseous inclusions (Fig. 8).

The density of methane in gaseous inclusions was also estimated from the Th values of a few of gaseous inclusions (Table 3). Although the Raman spectra reveal that there are small amount of CO_2 in the gaseous inclusions, no solid CO_2 was observed during the cooling and heating processes of gaseous inclusions. This is likely because that the CO_2 concentration in these inclusions are too minor to nucleate solid phases that are large enough for microscopic observation (van den Kerkhof, 1990). The Th values of the three types of gaseous inclusions range from −98.1 to −84.2 °C (Table 3), all below the critical temperature of methane (−82.1 °C). This phenomenon is an indicator of almost "pure" methane inclusion (i.e. CH_4 with less than 3 mol% CO_2) (Kisch et al., 1991), in which cases the effect of the presence of CO_2 is minor or negligible for the estimation of methane density using these Th values (Hashimoto et al., 2003).

The Th values of the selected type I gaseous inclusions are the lowest and range from −98.1 to −96.2 °C, which correspond to a methane density range of 0.293–0.300 g/cm^3 (Table 3). The respective Th values for type II and type III gaseous inclusions vary between −84.6 and −84.2 °C and −92.3 and −86.9 °C, from which the methane densities

were determined to be in the range of 0.224–0.229 g/cm^3 and 0.248–0.277 g/cm^3, respectively (Fig. 8). Although the Th-based methane density values are somewhat different from those by Raman shifts, they both illustrate that the methane in type I gaseous inclusions has the highest density for our samples.

4.4. Trapping pressure of type III gaseous inclusions

The trapping pressure of gaseous inclusions can be calculated by combining the methane density and trapping temperature, and the trapping temperature can be represented by the homogenization temperature of coeval two-phase aqueous inclusion (Parris et al., 2003; Fall et al., 2012; Bourdet et al., 2019). Considering that types I and II gaseous inclusions are derived from the secondary cracking of precursor oil inclusions, they cannot be used to calculate the trapping temperature and pressure using the technique mentioned above. Nevertheless the pressure calculated from them at the Th values of aqueous inclusions coeval with type III gaseous inclusions can serve as a proxy for the maximum pressure generated during oil to gas cracking in a closed system, which, when compared with the trapping pressures of type III gaseous inclusions, can be utilized to investigate whether or not the reservoirs were closed systems at the time.

Listed in Table 4 are the calculated pressures and formation pressure coefficients for selected type III gaseous inclusions whose coeval aqueous inclusions can be readily observed in the same microscopic

Table 4

Calculated trapping pressures of type III gaseous inclusions in samples GS102-3 and MX17-1 using their methane density and Th values as listed in Table 3. Also calculated were the internal pressures of types I and II gaseous inclusions based on their methane density range (Table 3) under the same temperatures as used for type III gaseous inclusions.

Sample	MX17-1	GS102-3	GS102-3	MX17-1	MX17-1	GS102-3	GS102-3
Trapping Temp (°C)	203.8	210.8	212.2	212.7	225.7	229.6	237.1
Trapping depth (km)	6.56	6.81	6.86	6.88	7.35	7.49	7.75
Pressure (MPa)[a]	—[g]	116.9–150.5/126.7	117.0–150.7/126.9	–	–	118.8–152.7/128.8	119.5–153.6/129.6
Pressure coefficient[a]	–	1.72–2.21/1.86	1.71–2.20/1.85	–	–	1.58–2.04/1.72	1.54–1.98/1.67
Pressure (MPa)[b]	–	91.2–118.8/103.5	91.2–118.9/103.7	–	–	92.7–120.7/105.3	93.3–121.5/106.0
Pressure coefficient[b]	–	1.34–1.74/1.52	1.33–1.73/1.51	–	–	1.24–1.61/1.41	1.20–1.57/1.37
Pressure (MPa)[c]	105.4–113.3/108.8	93.3–97.1/94.8	93.4–99.6/96.5	109.7–117.1/113.3	112.8–116.5/114.7	113.2–134.1/122.7	102.6–107.7/106.0
Pressure coefficient[c]	1.61–1.73/1.66	1.37–1.43/1.39	1.36–1.45/1.41	1.59–1.70/1.65	1.53–1.59/1.56	1.51–1.79/1.64	1.32–1.39/1.37
Pressure (MPa)[d]	–	150.5–159.4/155.5	150.7–159.6/155.7	–	–	152.7–161.7/157.8	153.6–162.6/158.7
Pressure coefficient[d]	–	2.21–2.34/2.28	2.20–2.33/2.27	–	–	2.04–2.16/2.10	1.98–2.10/2.05
Pressure (MPa)[e]	–	86.1–89.6/88.2	86.2–89.7/88.3	–	–	87.6–91.2/89.7	88.2–91.8/90.3
Pressure coefficient[e]	–	1.26–1.32/1.30	1.26–1.31/1.29	–	–	1.17–1.22/1.20	1.14–1.19/1.17
Pressure (MPa)[f]	117.0	–	–	116.1	–	111.4–134.1/123.7	112.1
Pressure coefficient[f]	1.78	–	–	1.69	–	1.49–1.79/1.65	1.45

[a] Calculated from the methane density of type I gaseous inclusions estimated by Raman shift of methane.
[b] Calculated from the methane density of type II gaseous inclusions estimated by Raman shift of methane.
[c] Calculated from the methane density of type III gaseous inclusions estimated by Raman shift of methane.
[d] Calculated from the methane density of type I gaseous inclusions estimated by homogenization temperature of gaseous inclusions.
[e] Calculated from the methane density of type II gaseous inclusions estimated by homogenization temperature of gaseous inclusions.
[f] Calculated from the methane density of type III gaseous inclusions estimated by homogenization temperature of gaseous inclusions.
[g] No data.

field. Using their Raman-shift-based methane densities, the trapping pressures of type III gaseous inclusions in samples GS102-3 and MX17-1 are in the range of 93.3–134.1 MPa and 105.4–117.1 MPa, respectively; in terms of their Th-based methane densities, the respective trapping pressures vary between 111.4 and 134.1 MPa and between 116.1 and 117.0 MPa (Fig. 9 and Table 4). It is worthy to note that the trapping pressures of these gaseous inclusions have a wide span, which was also reported by other studies and is likely attributed to fluctuation of reservoir pressure (Parris et al., 2003; Fall et al., 2012; Wang et al., 2014a; Gao et al., 2015; Li et al., 2018).

At the trapping temperatures of type III gaseous inclusions, the internal pressures of type I and type II gaseous inclusions were also estimated and the results are listed in Table 4. In terms of their Raman-based methane density values, the calculated internal pressures for type I gaseous inclusions range from 116.9 to 153.6 MPa, and from 91.2 to 121.5 MPa for type II gaseous inclusions (Table 4 and Fig. 9a). According to the Th-based methane density values, the calculated internal pressures for type I and type II gaseous inclusions are in the range of 150.5–162.6 MPa and 86.1–91.8 MPa, respectively (Table 4 and Fig. 9b). It is evident that the pressures in type I gaseous inclusions are much higher than those in type III gaseous inclusions. As mentioned earlier, the type III gaseous inclusions were formed during the time of natural gas accumulation, and therefore their trapping pressures can represent the reservoir pressures at their trapping time; by contrast, the internal pressures determined from type I gaseous inclusions at the trapping time of type III gaseous inclusions represent the maximum pressure that may be generated during oil to gas cracking in a closed system. It is worthy to note that the temperatures at which oils are cracked into dry gas (T$_{dry}$) may be lower than the temperatures recorded by the coeval aqueous fluid inclusions of type III gaseous inclusions, and thus the internal pressures in type I gaseous inclusions at T$_{dry}$ may be lower than those at the trapping temperature of type III gaseous

inclusions as listed in Table 4. However, the calculated internal pressures of type I gaseous inclusions only vary in a minor way when different T$_{dry}$ values are considered. For example, when the T$_{dry}$ temperatures drop from 237.1 °C to 210.8 °C, the internal pressures of type I gaseous inclusions drop from 119.5–153.6 MPa to 116.9–150.5 MPa (Table 4); even the T$_{dry}$ value drops to 200 °C, the reservoir pressures in a closed system as recorded by type I gaseous inclusions are still up to 115.6–149.1 MPa and higher than the reservoir pressures recorded by type III gaseous inclusions. Therefore, the reduced pressures by type III gaseous inclusions indicates that the paleo-oil reservoirs were not as closed as the precursor oil inclusions during the process of oil to gas cracking. Nevertheless the formation pressure coefficients calculated from type III gaseous inclusions are in the range of 1.32–1.79, implying that paleo-gas reservoirs at the time were still overpressured to varying extents.

5. Implications for the formation and evolution of gas pools

Based on the three different types of gaseous inclusions and the homogenization temperatures of their coeval aqueous inclusions, along with the presence of pyrobitumen inclusions, the formation and evolution of the present Sinan Dengying Formation gas pools can be divided into four stages (Figs. 10 and 11).

In the first stage, the present gas reservoirs were originally charged with oils, which is recorded by the type I gaseous inclusions and the pyrobitumen inclusions (Fig. 5a and e). Based on the Th values (120.3–136.9 °C) of aqueous inclusions coeval with type I gaseous inclusions and the thermal history of the fourth member of the Dengying Formation, the oil charge events occurred approximately 251–204 Ma in late Permian to Triassic (Figs. 10 and 11a).

The second stage was also related to oil charge events, forming type II precursor oil inclusions that were finally converted to the present type
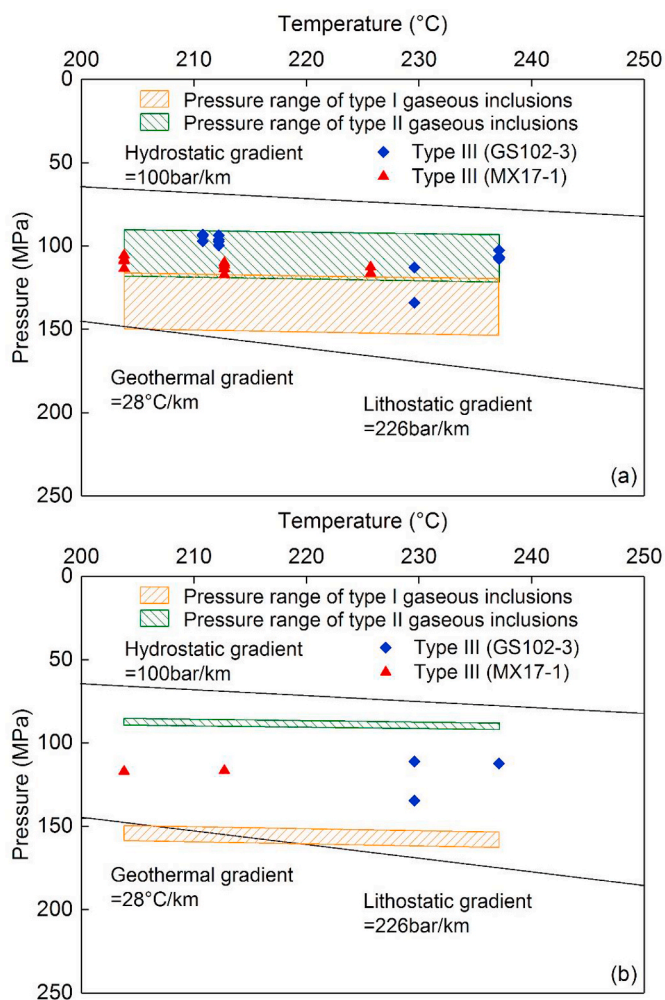
Fig. 9. Trapping temperatures and pressures of type III gaseous inclusions based on the Th values of their coeval aqueous inclusions and the methane density estimated from the methane Raman shift (a) and the Th value (b) of gaseous inclusions. The internal pressures of types I and II gaseous inclusions at the trapping temperatures of type III gaseous were also calculated according to the density values of methane in them. Only a few of Th values were collected for gaseous inclusions, and therefore the subfigure b should be treated with caution.
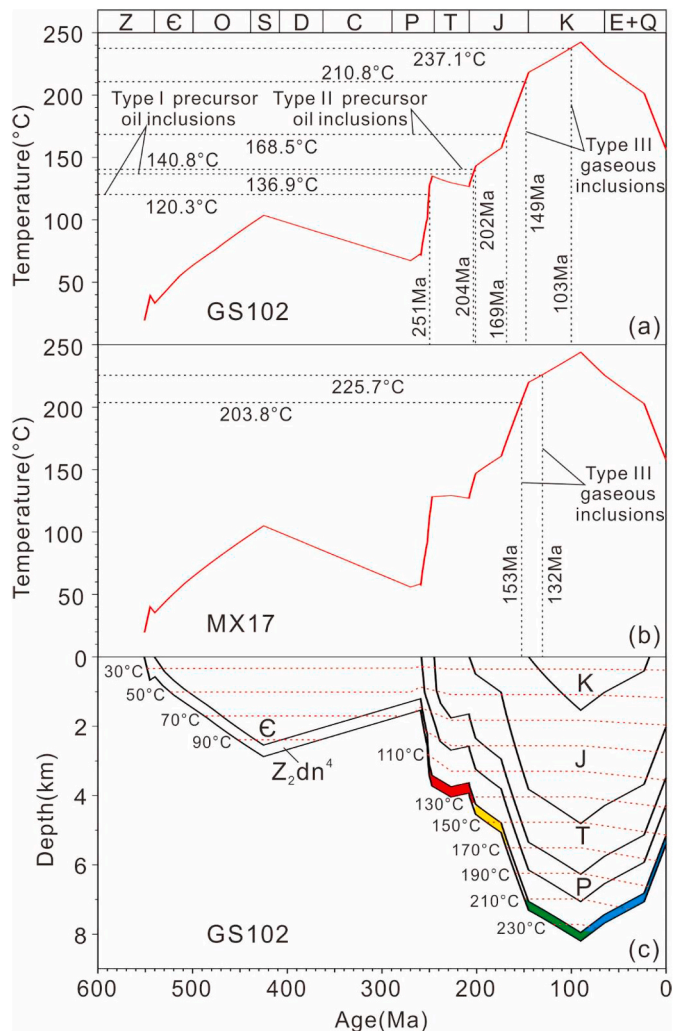

Fig. 10. The trapping time of the types I and II precursor oil inclusions and the type III gaseous inclusions. (a): Well GS102; (b): Well MX17 (b); and (c): the burial history and oil and gas accumulation history of the Sinian carbonate gas pool of well GS102. The thermal history was based on the resutls of Zhu et al. (2015) and Liu et al. (2018). Based on the thermal hisotry of Well GS102, the trapping time of type III gaseous inclusions cannot be unambiguously determined in terms of the Th vaules of their coeval aqueous inclusions; however the high methane densities observed in them (Table 4) indicate that they are most likely trapped during the burial stage rather than during the uplift stage.

II gaseous inclusions (Fig. 5b). Based on the Th values (140.8–168.5 °C) of their coeval aqueous inclusions, the second stage of oil charge events occurred during the time of 202–169 Ma in early-middle Jurassic (Figs. 10 and 11b).

The third stage is the main stage of gas accumulation as recorded by the type III gaseous inclusions. The Th values of aqueous inclusions identified in the xenomorphic quartz of samples GS102-3 and MX17-1 (Fig. 5c and d) reflect that type III gaseous inclusions were formed during the time of 153–103 Ma (Figs. 10 and 11c) when the paleo-oils had been converted to gas.

The fourth stage occurred about 90 Ma and continued to the present time due to the extensive tectonic uplift, during which the gas pool suffered somewhat destruction and adjustment (Fig. 11d; Sun et al., 2017; Luo et al., 2018), finally forming the present gas pool.

As illustrated earlier, although the Sinian reservoirs were overpressured during the oil to gas cracking stage as recorded by type III gaseous inclusions, it is now almost hydrostatically pressured with formation pressure coefficients of 1.06–1.14 (Liang et al., 2016). At the present burial depth of 5126.9 m for sample GS102-3, the reservoir has a pressure of around 56.5 MPa and a temperature of about 150 °C (Liu

et al., 2018). If the gas reservoir was kept intact (e.g., as closed as a fluid inclusion) and no methane was lost during tectonic uplift, the present pressures for sample GS102-3 would be 86.7–123.4 MPa, corresponding to formation pressure coefficients of 1.69–2.41, remarkably larger than the values of 1.32–1.79 (Table 4) when type III gaseous inclusions were trapped. This indicates that although the reservoir temperature and pressure decreased during the uplift stage, the pressure coefficient would increase drastically if the reservoirs were kept as closed as possible. At the present reservoir P-T conditions, the methane density is about 0.180 g/cm^3, which is much lower than the average methane density recorded by the type III gaseous inclusions for sample GS102-3 (0.244 g/cm^3) and sample MX17-1 (0.256 g/cm^3). To reach the present methane density of 0.180 g/cm^3, approximately 26–30% of the methane in reservoirs has to be dissipated since the time of type III gaseous inclusions were formed; alternatively the reservoir space has to be additionally supplemented by 36–42% during the tectonic uplift stage to reach the present methane density.

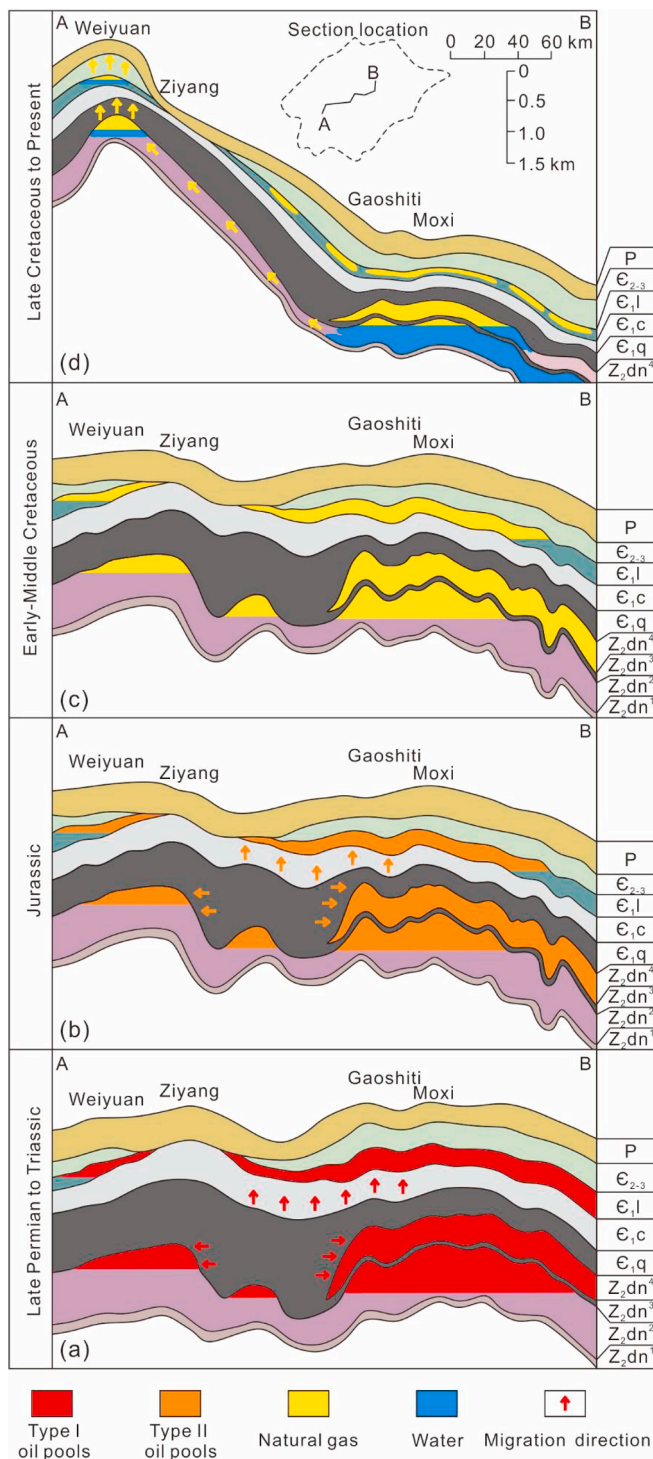Although there may be an increase in reservoir accommodation due

Fig. 11. Plots showing the evolution of Leshan-Longnvsi paleo-uplift and the four stages of oil and gas accumulation in the Sinian reservoirs (modified after Luo et al., 2018). (a): the formation of paleo-oil pools recorded by the type I gaseous inclusions that are derived from type I precursor oil inclusions formed during late Permian to Triassic; (b): the light or condensate oil stage of paleo-oil pools recorded by the type II gaseous inclusions that are derived from type II precursor oil inclusions trapped during Jurassic; (c): the stage of oil to gas cracking recorded by the type III gaseous inclusions during early to middle Cretaceous; (d): the stage of hydrostatic gas pools after late Cretaceous due to tectonic uplift.

to tectonic uplift, the increased volume by this mechanism is usually small and far less than 36–42% (Luo et al., 2015; Liu et al., 2016a; Xu et al., 2016). Thus it is more likely that the natural gas has migrated away and dissipated along the unconformities at the top of the reservoirs (Liang et al., 2016; Sun et al., 2017; Liu et al., 2018). During tectonic uplift stage, the WZ Bulge experienced a much more extensive uplift than the MG Bulge, and hence the natural gas in the MG Bulge might have migrated towards the WZ Bulge along the unconformities at the top of the Sinian reservoirs, finally transforming the overpressured reservoirs into the present almost hydrostatic reservoirs (Liang et al., 2016; Liu et al., 2018). It is worthy to note that the natural gas loss by vertical migration seem less significant than by lateral migration as the overlying Lower Cambrian gas pools are currently overpressured (Fig, 11d; Wang et al., 2014; Sun et al., 2017).

6. Conclusions

In the Sinian carbonate reservoirs of central Sichuan Basin, three types of methane-dominated inclusions were identified that have distinct geological significance. Both type I and type II methane-dominated inclusions contain various contents of pyrobitumen and are most likely derived from original oil inclusions, and thus they actually record the charging events of crude oils as well as oil cracking in a closed system. Type III methane-dominated inclusions, however, have no detectable pyrobitumen in them, and therefore they are formed by direct trapping of gases from contemporary gas pools and record the oil to gas cracking in reservoirs. This interpretation is further supported by the increasing homogenization temperatures of aqueous inclusions that are respectively coeval with type I, type II and type III methane-dominated inclusions.

Although the Sinian gas reservoirs are currently near-hydrostatic, the type III methane-dominated inclusions record paleo-overpressures with pressure coefficients of 1.32–1.79 in geological history. It is also suggested that the Sinian reservoirs were not as closed as oil inclusions during the time of oil to gas cracking because oil cracking in closed Sinian reservoirs would yield more extensive overpressures with pressure coefficients of 1.54–2.21 as estimated from type I methane-dominated inclusions. Therefore the loss of natural gas from the Sinian reservoirs may have occurred earlier than the strong tectonic uplift since the middle Cretaceous, which provides new clues to the search of secondary gas pools around the present Sinan gas pools.

significantly improved the whole quality of the manuscript.This is contribution No.IS-2954 from GIGCAS.

References

Barker, C., 1990. Calculated volume and pressure changes during the thermal-cracking of oil to gas in reservoirs. AAPG (Am. Assoc. Pet. Geol.) Bull. 74, 1254–1261.

Becker, S.P., Eichhubl, P., Laubach, S.E., Reed, R.M., Lander, R.H., Bodnar, R.J., 2010. A 48-m.y. history of fracture opening, temperature, and fluid pressure: Cretaceous Travis Peak Formation, East Texas Basin. Geol. Soc. Am. Bull. 122, 1081–1093.

Behar, F., Kressmann, S., Rudkiewicz, J.L., Vandenbroucke, M., 1992. Experimental simulation in a confined system and kinetic modelling of kerogen and oil cracking. Org. Geochem. 19, 173–189.

Bourdet, J., Heath, C.H., Kempton, R., 2019. Adaptation of Fluid Inclusion Techniques for Investigating Gas Charge - Examples from the Caswell Sub-basin, Browse Basin, Australia. Geological Society, London, Special Publications (in press).

Burruss, R.C., 1998. Evidence for petroleum occurrence and timing of migration: petroleum fluid inclusions, dead oil, stains, and seeps. In: The Oil and Gas Resource Potential of the 1002 Area, Arctic National Wildlife Refuge. U.S. Geological Survey Open-File Report, Alaska.

Burruss, R.C., 2003. Raman spectroscopy of fluid inclusions. In: Samson, I.M., et al. (Eds.), Fluid Inclusions: Analysis and Interpretation: Mineralogical Association of Canada Short Course Series, vol. 32, pp. 279–290.

Burruss, R.C., Slepkov, A.D., Pegoraro, A.F., Stolow, A., 2012. Unraveling the Complexity of Deep Gas Accumulations with Three-Dimensional Multimodal CARS Microscopy. Data Repository item, Geology, p. 2012310.

Chen, X., Simoneit, B.R.T., Wang, T.G., Ni, Z., Yuan, G.H., Chang, X.C., 2018. Molecular markers, carbon isotopes, and rare earth elements of highly mature reservoir pyrobitumens from Sichuan Basin, southwestern China: implications for PreCambrian-Lower Cambrian petroleum systems. Precambrian Res. 317, 33–56.

Chou, I.M., Song, Y.C., Hu, W.X., Burruss, R.C., Lu, W.J., 2006. A new method for synthesizing fluid inclusions containing organic and inorganic material. GSA Abstr. Progr. 38, 244.

Duan, J., Mei, Q., Li, B., Liang, Z., 2019. Sinian-early cambrian tectonic-sedimentary evolution in Sichuan Basin. Earth Sci. 44, 738–755.

Fall, A., Eichhubl, P., Cumella, S.P., Bodnar, R.J., Laubach, S.E., Becker, S.P., 2012. Testing the basin-centered gas accumulation model using fluid inclusion observations: southern Piceance Basin, Colorado. AAPG (Am. Assoc. Pet. Geol.) Bull. 96, 2297–2318.

Gao, J., He, S., Yi, J., 2015. Discovery of high density methane inclusions in Jiaoshiba shale gas field and its significance. Oil Gas Geol. 36 (3), 472–480 (in Chinese with English abstract).

Gao, P., Liu, G.D., Lash, G.G., Li, B.Y., Yan, D.T., Chen, C., 2018. Occurrences and origin of reservoir solid bitumen in sinian Dengying Formation dolomites of the Sichuan Basin, SW China. Int. J. Coal Geol. 200, 135–152.

Goldstein, R.H., 2001. Fluid inclusions in sedimentary and diagenetic systems. Lithos 55, 159–193.

Hashimoto, Y., Enjoji, M., Sakaguchi, A., Kimura, G., 2003. In situ pressure–temperature conditions of a tectonic mélange: constraints from fluid inclusion analysis of syn-mélange veins. Isl. Arc 12, 357–365.

Horsfield, B., Schenk, H.J., Mills, N., Welte, D.H., 1992. An investigation of the in-reservoir conversion of oil to gas: compositional and kinetic findings from closed-system programmed-temperature pyrolysis. Org. Geochem. 19, 191–204.

Huang, Y., Tarantola, A., Wang, W., Caumon, M.-C., Pironon, J., Lu, W., Yan, D., Zhuang, X., 2018. Charge history of CO_2 in Lishui sag, East China Sea basin: evidence from quantitative Raman analysis of CO_2-bearing fluid inclusions. Mar. Petrol. Geol. 98, 50–65.

Huc, A.Y., Nederlof, P., Debarre, R., Carpentier, B., Boussafir, M., Laggoun-Défarge, F., Lenail-Chouteau, A., Bordas-Le Floch, N., 2000. Pyrobitumen occurrence and formation in a cambro–ordovician sandstone reservoir, fahud salt basin, north Oman. Chem. Geol. 168, 99–112.

Liang, X., Liu, S., Xia, M., Sun, W., Deng, B., 2016. Characteristics and geological significance of gas chimney of the sinian Dengying Formation in the weiyuan structure, Sichuan Basin. Oil Gas Geol. 37, 702–712 (in Chinese with English abstract).

Lin, F., Bodnar, R.J., Becker, S.P., 2007. Experimental determination of the Raman CH_4 symmetric stretching (ν_1) band position from 1–650 bar and 0.3–22 °C: application to fluid inclusion studies. Geochem. Cosmochim. Acta 71, 3746–3756.

Liu, B., 2005. Thermal Dynamics of Hydrocarbon Inclusions (In Chinese). Science Press, Beijing.

Liu, D.H., Dai, J.X., Xiao, X.M., Tian, H., Yang, C., Hu, A.P., Mi, J.K., Song, Z.G., 2010. High density methane inclusions in Puguang Gasfield: discovery and a T-P genetic study. Chin. Sci. Bull. 54, 4714–4723.

Liu, Q.Y., Zhu, D.Y., Jin, Z.J., Liu, C.Y., Zhang, D.W., He, Z.L., 2016a. Coupled alteration of hydrothermal fluids and thermal sulfate reduction (TSR) in ancient dolomite reservoirs–An example from Sinian Dengying Formation in Sichuan Basin, southern China. Precambrian Res. 327, 1–13.

Liu, W., Qiu, N.S., Xu, Q.C., Liu, Y.F., 2018. Precambrian temperature and pressure system of Gaoshiti-Moxi block in the central paleo-uplift of Sichuan Basin, southwest China. Precambrian Res. 313, 91–108.

Liu, Y.F., Qiu, N.S., Xie, Z.Y., Yao, Q.Y., Zhu, C.Q., 2016b. Overpressure compartments in the central paleo-uplift, Sichuan Basin, southwest China. AAPG (Am. Assoc. Pet. Geol.) Bull. 100, 867–888.

Lu, W., Chou, I.M., Burruss, R.C., Song, Y., 2007. A unified equation for calculating methane vapor pressures in the CH_4–H_2O system with measured Raman shifts. Geochem. Cosmochim. Acta 71, 3969–3978.

Lüders, V., Plessen, B., 2015. Stable carbon isotope ratios of CH4-rich gas inclusions in shale-hosted fracture-fill mineralization: a tool for tracing hydrocarbon generation and migration in shale plays for oil and gas. Mar. Petrol. Geol. 63, 68–81.

Luo, B., Yang, Y., Luo, W.J., Wen, L., Wang, W.Z., Chen, K., 2015. Controlling factor and distribution of reservoir development in Dengying Formation of paleo-uplift in central Sichuan Basin. Acta Pet. Sin. 36, 416–426.

Luo, B., Yang, Y., Zhou, G., Luo, W.J., Shan, S.J., Xia, M.L., 2018. Basic characteristics and accumulation mechanism of Sinian–Cambrian giant highly mature and oil-cracking gas reservoirs in the Sichuan Basin, SW China. Energy Explor. Exploit. 36, 568–590.

Ma, Y.S., Guo, X.S., Guo, T.L., Huang, R., Cai, X.Y., Li, G.X., 2007. The Puguang gas field: new giant discovery in the mature Sichuan Basin, southwest China. AAPG (Am. Assoc. Pet. Geol.) Bull. 91, 627–643.

Mei, Q.H., He, D.F., Wen, Z., Li, Y.Q., Li, J., 2014. Geologic structure and tectonic evolution of Leshan-Longnvsi paleo-uplift in Sichuan Basin, China. Acta Pet. Sin. 35, 11–25 (in Chinese with English abstract).

Parris, T., Burruss, R., O'Sullivan, P., 2003. Deformation and the timing of gas generation and migration in the eastern Brooks range foothills, arctic national wildlife refuge, Alaska. AAPG (Am. Assoc. Pet. Geol.) Bull. 87, 1823–1846.

Rackett, H.G., 1970. Equation of state for saturated liquids. J. Chem. Eng. Data 15, 514–517.

Schenk, H.J., Di Primio, R., Horsfield, B., 1997. The conversion of oil into gas in petroleum reservoirs. Part 1: comparative kinetic investigation of gas generation from crude oils of lacustrine, marine and fluviodeltaic origin by programmed-temperature closed-system pyrolysis. Org. Geochem. 26, 467–481.

Schoenherr, J., Littke, R., Urai, J.L., Kukla, P.A., Rawahi, Z., 2007. Polyphase thermal evolution in the Infra-Cambrian Ara Group (South Oman Salt Basin) as deduced by maturity of solid reservoir bitumen. Org. Geochem. 38, 1293–1318.

Shi, C.H., Cao, J., Tan, X.C., Luo, B., Zeng, W., Hong, H.T., Huang, X., Wang, Y., 2018. Hydrocarbon generation capability of Sinian-Lower Cambrian shale, mudstone, and carbonate rocks in the Sichuan Basin, southwestern China: implications for contributions to the giant Sinian Dengying natural gas accumulation. AAPG (Am. Assoc. Pet. Geol.) Bull. 102, 817–853.

Song, J.M., Liu, S.G., Sun, W., Wu, W.H., Wang, G.Z., Peng, H.L., Tian, Y.H., Zhong, Y., 2013. Control of xingkai taphrogenesis on Dengying Formation high quality reservoirs in upper sinian of Sichuan Basin, China. J. Chengdu Univ. Technol. (Sci. Technol. Ed.) 40 (6), 658–670 (in Chinese with English abstract).

Sun, W., Liu, S.G., Song, J.M., Deng, B., Wang, G.Z., Wu, J., Jiao, K., Li, J.X., Ye, Y.H., Li, Z.W., Li, Z.Q., 2017. The formation process and characteristics of ancient and deep carbonate petroleum reservoirs in superimposed basins: a case study of Sinian (Ediacaran) Dengying Formation in the Sichuan superimposed basin, China. J. Chengdu Univ. Technol. (Sci. Technol. Ed.) 44, 257–285 (in Chinese with English abstract).

Thiéry, R., Pironon, J., Walgenwitz, F., Montel, F., 2000. PIT (Petroleum Inclusion Thermodynamic): a new modeling tool for the characterization of hydrocarbon fluid inclusions from volumetric and microthermometric measurements. J. Geochem. Explor. 69–70, 701–704.

Tian, H., Xiao, X.M., Wilkins, R.W.T., Tang, Y.C., 2008. New insights into the volume and pressure changes during the thermal cracking of oil to gas in reservoirs: implications for the in-situ accumulation of gas cracked from oils. AAPG (Am. Assoc. Pet. Geol.) Bull. 92, 181–200.

Tian, H., Xiao, X.M., Wilkins, R.W.T., Tang, Y.C., 2012. An experimental comparison of gas generation from three oil fractions: implications for the chemical and stable carbon isotopic signatures of oil cracking gas. Org. Geochem. 46, 96–112.

van den Kerkhof, A.M., 1990. Isochoric phase diagrams in the systems CO_2–CH_4 and CO_2–N_2: application to fluid inclusions. Geochem. Cosmochim. Acta 54, 621–629.

Vityk, M.O., Bodnar, R.J., 1995. Do fluid inclusions in high-grade metamorphic terranes preserve peak metamorphic density during retrograde decompression? Am. Mineral. 80, 641–644.

Volk, H., George, S.C., 2019. Using petroleum inclusions to trace petroleum systems – a review. Org. Geochem. 129, 99–123.

Wang, G.Z., Liu, S.G., Liu, W., Fan, L., Yuan, H.F., 2014a. Process of hydrocarbon accumulation of sinian Dengying Formation in gaoshiti structure, central sichuan, China. J. Chengdu Univ. Technol. (Sci. Technol. Ed.) 41, 684–693 (in Chinese with English abstract).

Wang, M.L., Xiao, X.M., Wei, Q., Zhou, Q., 2015. Thermal maturation of solid bitumen in shale as revealed by Raman spectroscopy. Natural Gas Geoscience 26, 1712–1718 (in Chinese with English abstract).

Wang, Z.C., Jiang, H., Wang, T.S., Lu, W.H., Gu, Z.D., Xu, A.N., Yang, Y., Xu, Z.H., 2014b. Paleo-geomorphology formed during Tongwan tectonization in Sichuan Basin and its significance for hydrocarbon accumulation. Petrol. Explor. Dev. 41, 305–312.

Waples, D.W., 2000. The kinetics of in-reservoir oil destruction and gas formation: constraints from experimental and empirical data, and from thermodynamics. Org. Geochem. 31, 553–575.

Wei, G.Q., Shen, P., Yang, W., Zhang, J., Jiao, G.H., Xie, W.R., Xie, Z.Y., 2013. Formation conditions and exploration prospects of Sinian large gas fields, Sichuan Basin. Petrol. Explor. Dev. 40, 139–149.

Wei, G.Q., Xie, Z.Y., Song, J.R., Yang, W., Wang, Z.H., Li, J., Wang, D.L., Li, Z.S., Xie, W.R., 2015a. Features and origin of natural gas in the sinian–cambrian of central sichuan paleo-uplift, Sichuan Basin, SW China. Petrol. Explor. Dev. 42, 768–777.

Wei, G.Q., Yang, W., Du, J.H., Xu, C.C., Zou, C.N., Xie, W.R., Wu, S.J., Zeng, F.Y., 2015b. Tectonic features of Gaoshiti-Moxi paleo-uplift and its controls on the formation of a giant gas field, Sichuan Basin, SW China. Petrol. Explor. Dev. 42, 283–292.

Xu, F.H., Xu, G.S., Liang, J.J., Yuan, H.F., Liu, Y., Xu, F.G., 2016. Multi-stage fluid charging and critical period of hydrocarbon accumulation of the sinian Dengying Formation in central Sichuan Basin. Acta Geologica Sinica-English Edition 90, 1549–1550.

Xu, H.L., Wei, G.Q., Jia, C.Z., Yang, W., Zhou, T.W., Xie, W.R., Li, C.X., Luo, B.W., 2012. Tectonic evolution of the Leshan-Longnvsi paleo-uplift and its control on gas accumulation in the Sinian strata, Sichuan Basin. Petroleum Explorarion and Development 39, 406–416.

Xu, Q.C., Qiu, N.S., Liu, W., Shen, A.J., Wang, X.F., 2018. Thermal evolution and maturation of sinian and cambrian source rocks in the central Sichuan Basin, southwest China. J. Asian Earth Sci. 164, 143–158.

Yang, C.Y., Ni, Z.Y., Li, M.J., Wang, T.G., Chen, Z.H., Hong, H.T., Tian, X.W., 2018. Pyrobitumen in South China: organic petrology, chemical composition and geological significance. Int. J. Coal Geol. 188, 51–63.

Yuan, Y.S., Sun, D.S., Li, S.J., Lin, J.H., 2013. Caledonian erosion thickness reconstruction in the Sichuan Basin. Chinese Journal of Geology 48, 581–591 (in Chinese with English abstract).

Zhang, J.L., Qiao, S.H., Lu, W.J., Hu, Q.C., Chen, S.G., Liu, Y., 2016. An equation for determining methane densities in fluid inclusions with Raman shifts. J. Geochem. Explor. 171, 20–28.

Zhang, S.C., He, K., Hu, G.Y., Mi, J.K., Ma, Q.S., Liu, K.Y., Tang, Y.C., 2018. Unique chemical and isotopic characteristics and origins of natural gases in the Paleozoic marine formations in the Sichuan Basin, SW China: isotope fractionation of deep and high mature carbonate reservoir gases. Mar. Petrol. Geol. 89, 68–82.

Zhao, W.Z., Zhang, S.C., Ke, K., Zeng, H.L., Hu, G., Zhang, B., Wang, Z.Y., Li, Y.X., 2018. Origin of conventional and shale gas in Sinian-lower Paleozoic strata in the Sichuan Basin: relayed gas generation from liquid hydrocarbon cracking. AAPG (Am. Assoc. Pet. Geol.) Bull. 103, 1265–1296.

Zhu, C.Q., Xu, M., Shan, J.N., Yuan, Y.S., Zhao, Y.Q., Hu, S.B., 2009. Quantifying the denudations of major tectonic events in Sichuan basin: constrained by the paleothermal records. Chin. Geol. 36 (6), 1268–1277.

Zhu, G.Y., Wang, T.S., Xie, Z.Y., Xie, B.H., Liu, K.Y., 2015. Giant gas discovery in the Precambrian deeply buried reservoirs in the Sichuan Basin, China: implications for gas exploration in old cratonic basins. Precambrian Res. 262, 45–66.

Zou, C.N., Du, J.H., Xu, C.C., Wang, Z.C., Zhang, B.M., Wei, G.Q., Wang, T.S., Yao, G.S., Deng, S.H., Liu, J.J., Zhou, H., Xu, A.N., Yang, Z., Jiang, H., Gu, Z.D., 2014a. Formation, distribution, resource potential, and discovery of Sinian–Cambrian giant gas field, Sichuan Basin, SW China. Petrol. Explor. Dev. 41 (3), 306–325.

Zou, C.N., Guo, J.L., Jia, A.L., Wei, Y.S., Yan, H.J., Jia, C.Y., Tang, H.F., 2020. Connotation of scientific development for gaint gas fields in China. Nat. Gas. Ind. 40 (3), 1–12 (in Chinese with English abstract).

Zou, C.N., Wei, G.Q., Xu, C.C., Du, J.H., Xie, Z.Y., Wang, Z.C., Hou, L.H., Yang, C., Li, J., Yang, W., 2014b. Geochemistry of the sinian–cambrian gas system in the Sichuan Basin, China. Org. Geochem. 74, 13–21.